

Exact flat bands in a 3D photonic crystal

Kin Hung Fung,¹ Yan-Long Chen,² C. T. Chan,^{1,*} and Qinghua Guo^{2,†}

¹*Department of Physics, The Hong Kong University of Science and Technology, Clear Water Bay, Kowloon, Hong Kong, China*

²*School of Physics and Electronics, Hunan University, Changsha, China*

(Dated: July 8, 2026)

Photonic flat bands are hard to engineer because Maxwell's equations are vectorial: transversality obstructs the localized scalar-like bases that generate destructive-interference flat bands in tight-binding models. We show that a three-dimensional metallic network of dipolar cavities joined by waveguide channels—a fully vectorial photonic crystal belonging to space group No. 224—hosts an exact scalar sector, carrying exact flat bands. The twelve-band vector problem contains one self-adaptive radial dipole axis per site whose projection is exactly the scalar four-band Hamiltonian of the same network. A microwave-scale coupled-dipole calculation confirms this scalar–vectorial duality. The result is a symmetry-based design rule for scalar-like flat bands in reciprocal vector media.

Introduction.—Flat bands concentrate an extensive density of states at a single frequency, and in tight-binding lattices they arise from a simple mechanism: on graphs with the right connectivity, amplitudes on the sublattices interfere destructively on every bond, giving compact localized eigenstates whose energy is independent of the Bloch wave vector \mathbf{k} [1, 2]. Photonic realizations are attractive because such a manifold enhances light–matter interaction, but electromagnetism imposes a structural obstruction: Maxwell's equations are vectorial and their solutions are transverse, so the localized scalar orbitals that underlie destructive-interference flat bands cannot be naively transplanted into a photonic crystal [3, 4]. The band-representation framework that classifies which bands a crystal can support [5–7] makes the obstruction precise: a set of photonic bands is scalar-like only if it is induced from a one-dimensional site representation, and vector site symmetry generically forbids this. Whether a lattice *graph* has flat bands is therefore settled at the scalar level, by connectivity alone; the question we answer is whether a genuine *vector* photonic crystal carries the same flat bands as exact eigenstates rather than letting transversality wash them out.

Here we present a three-dimensional metallic photonic crystal in which this occurs, and identify the exact condition under which the scalar and vector descriptions coincide. The crystal is a space-group-224 ($Pn\bar{3}m$) network of spherical metallic cavities connected by narrow waveguide channels; each cavity contributes its lowest electric-dipolar Maxwell triplet, so the reduced problem is a twelve-band vector Hamiltonian. We single out one self-adaptive radial dipole axis on each of the four sublattices and show, analytically, that the projection of the twelve-band operator onto these four axes is *always* a rescaled copy of the scalar four-band Hamiltonian of the same network. The rescaling is a single geometric number set by the longitudinal and transverse channel couplings. This projected sector inherits the two flat bands of the scalar model, but a projected flat band need not be a flat band of the full vector operator. We prove that the

projected branches are exact full-vector eigenstates if and only if the longitudinal and transverse channel couplings are equal in magnitude and opposite in sign, at which point every bond acts as a Householder reflection that maps the radial axis at one end of the bond onto the radial axis at the other. A microwave-scale coupled-dipole computation confirms these results. The construction is a concrete instance of scalar–vectorial duality and supplies a symmetry-based recipe for exact flat bands in reciprocal vector media.

Model.—The crystal is a metallic space-group-224 network. The four sites form a Wyckoff orbit of $Pn\bar{3}m$ —a *primitive*-cubic space group whose sites carry the non-centrosymmetric tetrahedral point symmetry $\bar{4}3m$ —and occupy the cubic-cell positions $\mathbf{r}_A = (0, 0, 0)$, $\mathbf{r}_B = (0, \frac{1}{2}, \frac{1}{2})$, $\mathbf{r}_C = (\frac{1}{2}, 0, \frac{1}{2})$ and $\mathbf{r}_D = (\frac{1}{2}, \frac{1}{2}, 0)$, each pair joined by a straight metallic channel along one of the six face-diagonal directions

$$\begin{aligned} \hat{\mathbf{n}}_{AB} &= \frac{(0,1,1)}{\sqrt{2}}, & \hat{\mathbf{n}}_{AC} &= \frac{(1,0,1)}{\sqrt{2}}, & \hat{\mathbf{n}}_{AD} &= \frac{(1,1,0)}{\sqrt{2}}, \\ \hat{\mathbf{n}}_{BC} &= \frac{(1,-1,0)}{\sqrt{2}}, & \hat{\mathbf{n}}_{BD} &= \frac{(1,0,-1)}{\sqrt{2}}, & \hat{\mathbf{n}}_{CD} &= \frac{(0,1,-1)}{\sqrt{2}}. \end{aligned} \quad (1)$$

The retained degree of freedom at each site is not an abstract orbital: it is the lowest electric-dipolar (TM, $\ell = 1$) triplet of a spherical perfect-conductor reference cavity, whose first dipolar resonance Ω_0 lies below the magnetic-dipolar (TE) triplet (Appendix A). Projecting the frequency-domain Maxwell problem onto these triplets and eliminating the channel fields and higher cavity modes gives a coupled-dipole eigenproblem for the twelve-component amplitude $\mathbf{a}(\mathbf{k}) = (\mathbf{a}_A, \mathbf{a}_B, \mathbf{a}_C, \mathbf{a}_D)^\top$,

$$[\mathbf{I}_{12} - g H(\mathbf{k})] \mathbf{a} = \left(\frac{\Omega}{\Omega_0}\right)^2 \mathbf{a}, \quad \lambda(\mathbf{k}) = \frac{1 - (\Omega/\Omega_0)^2}{g}, \quad (2)$$

so that the band frequency is $\Omega_n(\mathbf{k})/\Omega_0 = \sqrt{1 - g \lambda_n(\mathbf{k})}$. Here $H(\mathbf{k})$ is the dimensionless shift operator, Ω_0 the isolated-cavity resonance, and g the coupling-smallness parameter; the eigenvalue λ plays the role of the frequency-squared shift, and the reduction is detailed in

Appendix A. The operator is fixed by two ingredients. The on-site block encodes a local radial anisotropy of strength Δ_χ , carried by the tensor polarizability of the cavity dipole (not by any tensor permittivity),

$$\Sigma_u = \Delta_\chi \hat{\chi}_u \hat{\chi}_u^\top, \quad (3)$$

along the self-adaptive radial axis of sublattice u ,

$$\begin{aligned} \hat{\chi}_A &= -\frac{(1,1,1)}{\sqrt{3}}, & \hat{\chi}_B &= \frac{(-1,1,1)}{\sqrt{3}}, \\ \hat{\chi}_C &= \frac{(1,-1,1)}{\sqrt{3}}, & \hat{\chi}_D &= \frac{(1,1,-1)}{\sqrt{3}}. \end{aligned} \quad (4)$$

The staggered signs in Eq. (4) are fixed by the $\bar{4}3m$ site symmetry, which selects a single polar radial axis on each site; this polar on-site direction exists only because $Pn\bar{3}m$ sites are noncentrosymmetric—a point we return to below, as it is what distinguishes the present crystal from a face-centered-cubic one. The channel block on a bond of unit direction $\hat{\mathbf{n}}$ is the reciprocal bond tensor

$$\mathcal{J}(\hat{\mathbf{n}}) = J_T(\mathbf{I}_3 - \hat{\mathbf{n}}\hat{\mathbf{n}}^\top) + J_L \hat{\mathbf{n}}\hat{\mathbf{n}}^\top, \quad (5)$$

where the longitudinal coupling J_L and transverse coupling J_T refer to the local channel axis, not to a global polarization or to \mathbf{k} : no nonreciprocal hopping is inserted anywhere (Appendix B). With the scalar Bloch factors

$$\begin{aligned} h_{AB} &= 1 + e^{-i(k_y+k_z)}, & h_{AC} &= 1 + e^{-i(k_x+k_z)}, \\ h_{AD} &= 1 + e^{-i(k_x+k_y)}, & h_{BC} &= 1 + e^{-i(k_x-k_y)}, \\ h_{BD} &= 1 + e^{-i(k_x-k_z)}, & h_{CD} &= 1 + e^{-i(k_y-k_z)}, \end{aligned} \quad (6)$$

the twelve-band vector Hamiltonian is the Hermitian block matrix

$$H(\mathbf{k}) = \begin{pmatrix} \Sigma_A & \mathcal{J}_{AB}h_{AB} & \mathcal{J}_{AC}h_{AC} & \mathcal{J}_{AD}h_{AD} \\ \mathcal{J}_{AB}^\top h_{AB}^* & \Sigma_B & \mathcal{J}_{BC}h_{BC} & \mathcal{J}_{BD}h_{BD} \\ \mathcal{J}_{AC}^\top h_{AC}^* & \mathcal{J}_{BC}^\top h_{BC}^* & \Sigma_C & \mathcal{J}_{CD}h_{CD} \\ \mathcal{J}_{AD}^\top h_{AD}^* & \mathcal{J}_{BD}^\top h_{BD}^* & \mathcal{J}_{CD}^\top h_{CD}^* & \Sigma_D \end{pmatrix}, \quad (7)$$

with $\mathcal{J}_{uv} \equiv \mathcal{J}(\hat{\mathbf{n}}_{uv})$. The geometry of the network is shown in Fig. 1(a).

Scalar reference and radial projection.—The same network defines a scalar four-band Hamiltonian $H_{\text{sc}}(\mathbf{k})$ whose off-diagonal entries are the Bloch factors of Eq. (6) (the reference hopping is set to unity, so H_{sc} and its eigenvalues are dimensionless) and whose diagonal vanishes. Its spectrum contains two exactly flat bands,

$$\lambda_{\text{sc},1}(\mathbf{k}) = \lambda_{\text{sc},2}(\mathbf{k}) = -2, \quad (8)$$

together with two dispersive bands; the flat pair is the destructive-interference manifold of the four-site graph. We now examine how much of this scalar physics survives in the vector operator (7). Collect the four radial axes into the 12×4 isometry

$$Q = \text{diag}(\hat{\chi}_A, \hat{\chi}_B, \hat{\chi}_C, \hat{\chi}_D), \quad Q^\top Q = \mathbf{I}_4, \quad (9)$$

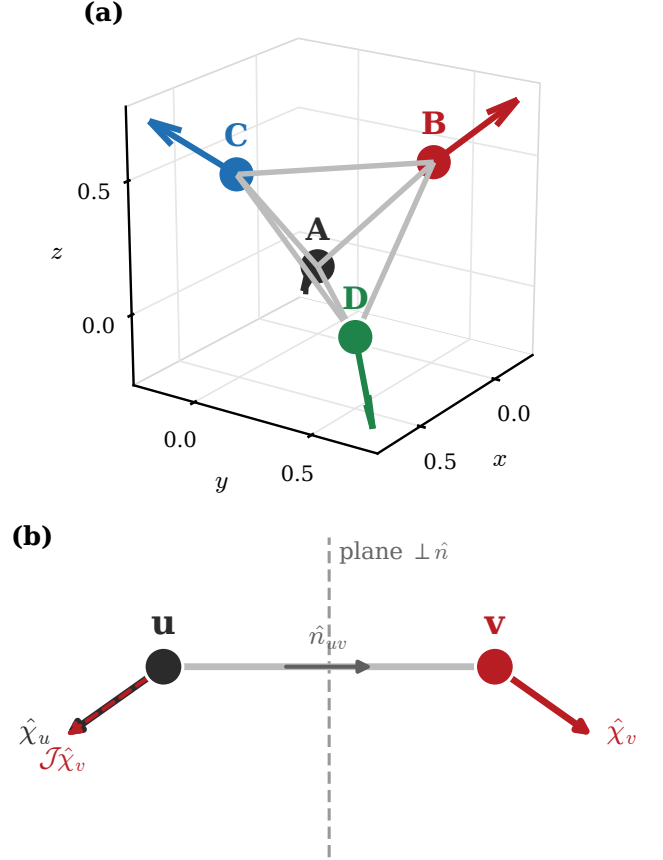


FIG. 1. (a) The metallic space-group-224 network: four cavities A, B, C, D at the $\bar{4}3m$ Wyckoff sites of $Pn\bar{3}m$ in the cubic cell, six face-diagonal channels, and the self-adaptive radial dipole axes $\hat{\chi}_u$ of Eq. (4) (arrows). (b) Exchange mechanism at the balance $J_L = -J_T$. There the bond tensor $\mathcal{J}(\hat{\mathbf{n}}) = J_T(\mathbf{I}_3 - 2\hat{\mathbf{n}}\hat{\mathbf{n}}^\top)$ is J_T times the Householder reflection about the plane $\perp \hat{\mathbf{n}}$; because the radial axes obey $\hat{\chi}_v - \hat{\chi}_u = 2\sqrt{2/3} \hat{\mathbf{n}}_{uv}$, this reflection sends $\hat{\chi}_v \mapsto \hat{\chi}_u$, so a channel maps the radial dipole at one end of a bond onto the radial dipole at the other (up to the overall coupling J_T).

so that QQ^\top is the rank-four projector onto the radial subspace. The construction rests on three bond-independent identities obeyed by (1) and (4) for every oriented bond $u \rightarrow v$,

$$\hat{\mathbf{n}}_{uv} \cdot \hat{\chi}_v = \sqrt{\frac{2}{3}}, \quad \hat{\mathbf{n}}_{uv} \cdot \hat{\chi}_u = -\sqrt{\frac{2}{3}}, \quad \hat{\chi}_u \cdot \hat{\chi}_v = -\frac{1}{3}, \quad (10)$$

equivalently $\hat{\chi}_v - \hat{\chi}_u = 2\sqrt{2/3} \hat{\mathbf{n}}_{uv}$: the bond axis points along the chord joining the two local radial orientations. A one-line computation using (10) gives the projected radial matrix element $\hat{\chi}_u^\top \mathcal{J}(\hat{\mathbf{n}}_{uv}) \hat{\chi}_v = (J_T - 2J_L)/3$, while the on-site term contributes $\hat{\chi}_u^\top \Sigma_u \hat{\chi}_u = \Delta_\chi$. Hence, for any channel couplings,

$$Q^\top H(\mathbf{k}) Q = \Delta_\chi \mathbf{I}_4 + J_\chi H_{\text{sc}}(\mathbf{k}), \quad J_\chi = \frac{J_T - 2J_L}{3}. \quad (11)$$

The radial projection of the vector crystal is exactly the

scalar crystal, shifted by the anisotropy and rescaled by the single geometric factor J_χ . In particular the projected sector carries two flat guide branches at $\lambda_{\chi,\text{flat}} = \Delta_\chi - 2J_\chi$, inherited from Eq. (8).

Scalar-vectorial duality.—Equation (11) concerns the projected block only; a flat branch of $Q^\top H Q$ is a flat band of the full operator H only if the radial subspace does not leak into its complement. Acting with a bond tensor on the radial axis at the far end of a bond and using (10),

$$\mathcal{J}(\hat{\mathbf{n}}_{uv})\hat{\chi}_v = J_T\hat{\chi}_u + \sqrt{\frac{2}{3}}(J_L + J_T)\hat{\mathbf{n}}_{uv}. \quad (12)$$

The first term lands on the target radial axis; the second is an off-radial component along $\hat{\mathbf{n}}_{uv}$, which is not parallel to $\hat{\chi}_u$. It vanishes on every bond if and only if $J_L + J_T = 0$, i.e.

$$(\mathbf{I}_{12} - Q Q^\top)H(\mathbf{k})Q = 0 \iff J_L = -J_T. \quad (13)$$

At this balance the radial subspace is an exact invariant subspace of the twelve-band Hamiltonian (Appendix C): its four eigenbands are precisely the projected bands of Eq. (11), and the two projected flat branches become two exact full-vector flat bands at $\lambda = \Delta_\chi - 2J_\chi$ (with $J_\chi = J_T$ at the balance). The balance has a transparent geometric meaning. Writing $J_L = -J_T$, the bond tensor factorizes as

$$\mathcal{J}(\hat{\mathbf{n}}) = J_T(\mathbf{I}_3 - 2\hat{\mathbf{n}}\hat{\mathbf{n}}^\top), \quad (14)$$

J_T times the Householder reflection about the plane orthogonal to $\hat{\mathbf{n}}$. Because $\hat{\chi}_v - \hat{\chi}_u \parallel \hat{\mathbf{n}}_{uv}$, this reflection exchanges the endpoint radial axes, $\mathcal{J}(\hat{\mathbf{n}}_{uv})\hat{\chi}_v = J_T\hat{\chi}_u$ and $\mathcal{J}(\hat{\mathbf{n}}_{uv})\hat{\chi}_u = J_T\hat{\chi}_v$ [Fig. 1(b)]. The scalar destructive-interference pattern is thereby carried, without residue, by a purely reciprocal vector coupling: the local anisotropy Δ_χ supplies the spectral separation, and the balance $J_L = -J_T$ supplies exact decoupling.

Numerical demonstration.—We verify the duality with a microwave-scale coupled-dipole calculation at fixed anisotropy $\Delta_\chi = -20$ and coupling parameter $g = 0.03$, with the channel couplings measured in units of the transverse coupling (at the balance the realized radial coupling is $J_\chi = J_T$). Diagonalizing Eq. (7) along $\Gamma \rightarrow X \rightarrow M \rightarrow R \rightarrow \Gamma$ and mapping to frequency through Eq. (2) gives the band structures of Fig. 2. Displayed in its own eigenvalue with the same coupling sign as the realized radial sector ($J_\chi = J_T$), the scalar four-band reference $H_{\text{sc}}(\mathbf{k})$ shows two flat bands at $\lambda_{\text{sc}} = -2$ and two dispersive bands [Fig. 2(a)]. A negative Δ_χ lowers the radial manifold in λ but, through the decreasing frequency map, raises it in frequency, so at the balance $J_L = -J_T$ the four radial bands (crimson) detach above the remaining eight (grey) across a frequency gap [Fig. 2(b)]. These four bands coincide with the projected scalar bands $\Delta_\chi\mathbf{I}_4 + H_{\text{sc}}(\mathbf{k})$ of Eq. (11) to machine precision: two are

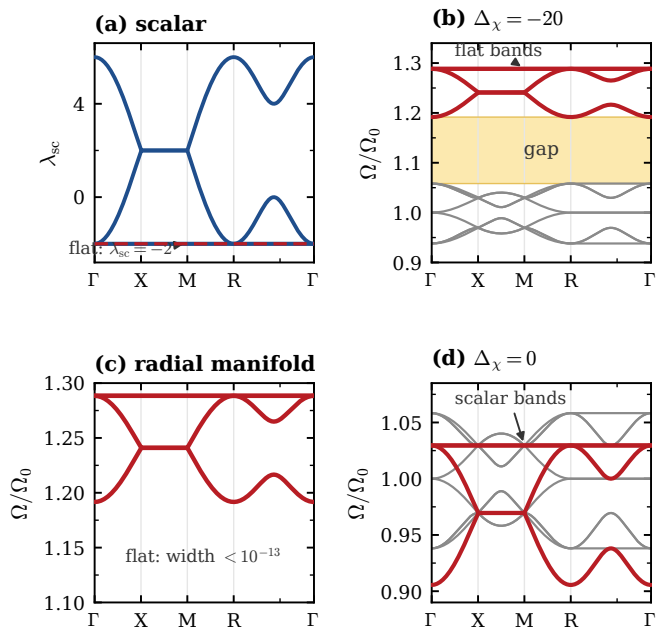


FIG. 2. Scalar reference and exact vector flat bands of the space-group-224 network along $\Gamma \rightarrow X \rightarrow M \rightarrow R \rightarrow \Gamma$. (a) The scalar four-band Hamiltonian $H_{\text{sc}}(\mathbf{k})$ in its eigenvalue λ_{sc} : two flat bands at $\lambda_{\text{sc}} = -2$ (dashed) and two dispersive bands. It is plotted with the same coupling sign as the realized radial sector ($J_\chi = J_T$ at balance); because the frequency map $\Omega/\Omega_0 = \sqrt{1 - g\lambda}$ is decreasing, the corresponding vector radial bands in (b),(c) appear with the flat pair at the *top*. (b) Full twelve-band vector spectrum at $\Delta_\chi = -20$ and the balance $J_L = -J_T$: four radial bands (crimson, $= \Delta_\chi\mathbf{I}_4 + H_{\text{sc}}(\mathbf{k})$ of Eq. (11)) detach above the eight remaining vector bands (grey) across a frequency gap (shaded), and two of them are exactly flat at $\Omega/\Omega_0 = 1.28841$. (c) The isolated SG224 radial manifold of (b): two exactly flat bands (residual bandwidth $< 10^{-13}$) and two dispersive radial bands, reproducing the band shape of the scalar reference (a). (d) Without anisotropy ($\Delta_\chi = 0$) the four scalar bands (crimson) remain exact eigenstates at balance but overlap the eight transverse bands (grey), so the scalar sector is present yet not spectrally isolated. Frequencies use $g = 0.03$; (a) is the dimensionless scalar shift eigenvalue λ_{sc} (reference hopping set to unity); (b)–(d) are frequencies in units of Ω_0 .

perfectly flat at $\Omega/\Omega_0 = \sqrt{1 - g(\Delta_\chi - 2)} = 1.28841$ and two disperse, reproducing the shape of the scalar reference, with a residual flat-band width below 10^{-13} across the zone [Fig. 2(c)]. Without anisotropy the twelve vector bands overlap and no radial sector is isolated [Fig. 2(d)].

The exactness of the duality is a matter of site symmetry, and it is visible directly in the bands. With the $43m$ -adapted axes of Eq. (4) the balanced crystal carries four radial bands of unit radial weight, two of them perfectly flat [Fig. 3(a,c)], so the projected scalar sector is realized as exact full-vector eigenstates; the balance and two neighboring imbalances are compared in Table I. Replacing the staggered axes by a single common (FCC-equivalent) axis on every site—the pattern the higher

symmetry of $Fm\bar{3}m$ would enforce—destroys both features: the detached sector disperses and its weights are no longer quantized [Fig. 3(b,d)], so no exact scalar band remains. The reason is structural: $Fm\bar{3}m$ would render the four sites equivalent, collapsing the four-sublattice interference graph to a single primitive site, and would impose a centrosymmetric $m\bar{3}m$ site symmetry that forbids the polar radial axis altogether; the staggered axes exist only because $Pn\bar{3}m$ is a primitive-cubic group with noncentrosymmetric sites. The anisotropy Δ_χ plays a separate role: it opens a radial–bulk frequency gap for sufficiently strong anisotropy, isolating the radial manifold spectrally [seen at $\Delta_\chi = -20$ in Fig. 3(a,b)], a knob independent of the balance.

Discussion.—The two identities (11) and (13) separate the physics into an always-true statement and a resonance condition. Equation (11) says the radial projection of this vector crystal is *always* the scalar crystal, rescaled by $J_\chi = (J_T - 2J_L)/3$; the scalar destructive-interference flat bands are therefore visible as projected guide branches for any coupling. Equation (13) says these branches lift to exact full-vector flat bands only at $J_L = -J_T$, when each bond is a Householder reflection exchanging the radial axes it connects. This is a clean example of scalar–vectorial duality: one self-adaptive orbital per site—an “orbital half” of the dipolar triplet—realizes a full scalar band representation inside a transverse vector medium, but only when the reciprocal channel tensor is tuned to reflect rather than merely transmit. The design rule is practical. The anisotropy Δ_χ is an on-site splitting that isolates the radial manifold spectrally and is easy to realize by shaping the cavity; the balance $J_L = -J_T$ is a channel property fixed by the waveguide geometry (Appendix B), so the two knobs are independent. Flat photonic bands have been realized before—in three dimensions from the internal mode

TABLE I. Channel-balance comparison at $\Delta_\chi = -20$, $g = 0.03$, channel couplings in units of the transverse coupling, for three channel balances (columns). Rows: the geometric-factor ratio J_χ/J_T with $J_\chi = (J_T - 2J_L)/3$; the exchange residual $r_{\mathcal{J}} = \max_{uv} \|\mathcal{J}(\hat{\mathbf{n}}_{uv})\hat{\chi}_v - \hat{\chi}_u\|$; the bare-scalar projection residual $r_{\text{sc}} = \max_{\mathbf{k}} \|Q^T H Q - (\Delta_\chi \mathbf{I}_4 + H_{\text{sc}})\|$; the off-sector residual $r_\perp = \max_{\mathbf{k}} \|(\mathbf{I}_{12} - Q Q^T) H Q\|$; the radial-band frequency window Ω_χ/Ω_0 ; and the radial–bulk frequency gap. Only $J_L = -J_T$ gives exact vector flat bands.

J_L/J_T	-2	0	-1
J_χ/J_T	5/3	1/3	1
$r_{\mathcal{J}}$	0.8165	0.8165	3×10^{-16}
r_{sc}	4.619	4.619	2×10^{-14}
r_\perp	3.266	3.266	2×10^{-14}
Ω_χ/Ω_0	[1.140, 1.304]	[1.241, 1.273]	[1.192, 1.288]
gap $\Delta(\Omega/\Omega_0)$	0.068	0.197	0.133
flat bands	projected	projected	exact (2)

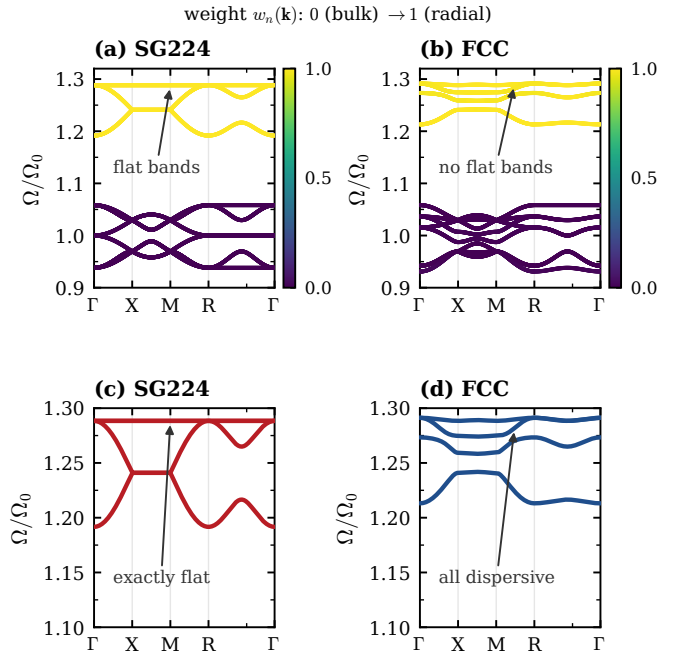


FIG. 3. Symmetry origin of the exact scalar sector, shown through band physics ($\Delta_\chi = -20$, $g = 0.03$, $J_L = -J_T$). (a) Vector bands with the $Pn\bar{3}m$ ($43m$) radial axes of Eq. (4), colored by radial weight $w_n(\mathbf{k}) = \|Q^T \psi_n(\mathbf{k})\|^2$: four radial bands of unit weight detach above the gap and two of them are exactly flat—the projected scalar sector realized as full-vector eigenstates. (b) The same crystal with a single common (FCC-equivalent) radial axis on every site: the detached sector disperses and its weights are no longer quantized, so no exact scalar band survives. (c) Zoom on the SG224 radial manifold of (a): two exactly flat bands (residual bandwidth $< 10^{-13}$) and two dispersive bands. (d) Zoom on the FCC-equivalent radial manifold of (b) at the same anisotropy: four dispersive bands and no flat band. Panels (a) and (b) share the weight colorbar; (c) and (d) share the frequency axis.

degeneracy of metallic meta-atoms [17], and more generally by band engineering beyond the tight-binding picture [18]—but there the flatness is approximate and set by the meta-atom or the microstructure. Here it is *exact*: the zero bandwidth is guaranteed by the projection identity (11) and is switched on only by tuning the coupling to the reciprocal balance $J_L = -J_T$, independent of the cavity details. Everything here uses only reciprocal, passive ingredients realizable on a standard microwave metallic platform, and the mechanism transfers to any vector lattice whose site-adapted axes obey a chord identity of the form (10). More broadly, the result shows that band-representation obstructions to scalar-like photonic bands [3, 5, 6] can be met not by abandoning the vector character of Maxwell’s equations but by arranging the couplings so that a chosen orbital sector closes exactly onto itself.

This work was supported by the Research Grants Council of Hong Kong (16310422), and by the Hunan

University.

Appendix A: Maxwell reduction and TE/TM convention

The microscopic object at each site is a spherical metallic cavity, connected to its neighbors by metallic waveguide channels. Its normal modes solve the Maxwell cavity eigenproblem $\nabla \times \mu^{-1} \nabla \times \mathbf{e}_s = (\omega_s^2/c^2) \epsilon \mathbf{e}_s$ with the perfect-conductor condition $\hat{\mathbf{n}} \times \mathbf{e}_s = 0$ on the boundary [8, 9, 14]. Organizing the modes with vector spherical harmonics separates them into electric (TM) and magnetic (TE) multipoles [10, 11]; the $\ell = 1$ electric multipole is the electric-dipole (a_1) coefficient and the $\ell = 1$ magnetic multipole the magnetic-dipole (b_1) coefficient. For a perfect spherical metal cavity the characteristic equations are $\frac{d}{dx}[xj_\ell(x)] = 0$ (TM) and $j_\ell(x) = 0$ (TE); the lowest dipolar roots are

$$x_{1,1}^{\text{TM}} = 2.7437\dots, \quad x_{1,1}^{\text{TE}} = 4.4934\dots, \quad (\text{A1})$$

so the electric-dipolar TM triplet is the lowest dipolar triplet and is used as the site basis; its threefold-degenerate $m = -1, 0, 1$ states form the Cartesian dipole triplet with reference resonance Ω_0 [9, 12]. The material permittivity is treated as a scalar throughout; the anisotropy of the effective model is carried entirely by the tensor polarizability of the cavity dipole,

$$\boldsymbol{\alpha}_u^{-1}(\omega) = \frac{1}{\mathcal{A}} [(\Omega_0^2 - \omega^2) \mathbf{I}_3 - g \Omega_0^2 \Delta_\chi \hat{\boldsymbol{\chi}}_u \hat{\boldsymbol{\chi}}_u^\top], \quad (\text{A2})$$

whose anisotropic part defines Δ_χ [15, 16]. In the absence of an external source the per-site dipole amplitudes \mathbf{a}_u obey the coupled-dipole eigenmode condition

$$\boldsymbol{\alpha}_u^{-1}(\omega) \mathbf{a}_u = \sum_v h_{uv}(\mathbf{k}) \mathbf{G}_{uv}^{\text{ch}} \mathbf{a}_v, \quad (\text{A3})$$

where $h_{uv}(\mathbf{k})$ is the Bloch sum of Eq. (6) over the bonds joining sublattices u and v and $\mathbf{G}_{uv}^{\text{ch}}$ is the channel Green tensor of Appendix B. Multiplying Eq. (A3) by $\mathcal{A}/(g\Omega_0^2)$ and using the dimensionless couplings $J_{L,T}$ defined there, the isotropic part yields the frequency-squared shift $\lambda = (1 - \omega^2/\Omega_0^2)/g$, the anisotropic on-site part collapses to $\Sigma_u = \Delta_\chi \hat{\boldsymbol{\chi}}_u \hat{\boldsymbol{\chi}}_u^\top$, and the bond part to $\mathcal{J}(\hat{\mathbf{n}}_{uv}) h_{uv}(\mathbf{k})$. Equation (A3) is then exactly the eigenproblem (2) with the operator (7) and band frequencies $\Omega_n/\Omega_0 = \sqrt{1 - g\lambda_n}$. The same Ω_0 and g appear in the polarizability, in the couplings, and in the frequency map, so the Lorentz-oscillator normalization is common to every equation.

Appendix B: Channel Green tensor and the couplings J_L, J_T

For a straight channel of axis $\hat{\mathbf{n}}_{uv}$, rotational symmetry about the axis restricts the projected Green tensor in the

retained dipolar subspace to $\mathbf{G}_{uv}^{\text{ch}} = G_L \hat{\mathbf{n}}_{uv} \hat{\mathbf{n}}_{uv}^\top + G_T (\mathbf{I}_3 - \hat{\mathbf{n}}_{uv} \hat{\mathbf{n}}_{uv}^\top)$ [8, 12], giving one coefficient for a dipole along the channel and one for either transverse orientation. The dimensionless couplings are $J_{L,T} = (\mathcal{A}/g\Omega_0^2) G_{L,T}$, and for the symmetry-equivalent bonds of the network they are site independent, so the channel block is Eq. (5). A waveguide-mode estimate fixes their ratio: below cutoff the dominant contributions come from the lowest evanescent channel modes, with G_T controlled by the TE_{11} -like mode and G_L by the TM_{01} -like mode [12, 13], so that

$$\frac{J_L}{J_T} \simeq \frac{C_L}{C_T} \frac{\gamma_{\text{TE11}}}{\gamma_{\text{TM01}}} e^{-(\gamma_{\text{TM01}} - \gamma_{\text{TE11}}) \ell_{\text{ch}}}, \quad (\text{B1})$$

with cutoff constants $\gamma_{\text{TE11}} = [(1.8412/a_{\text{ch}})^2 - \epsilon_{\text{ch}} \mu_{\text{ch}} \Omega_0^2/c^2]^{1/2}$ and $\gamma_{\text{TM01}} = [(2.4048/a_{\text{ch}})^2 - \epsilon_{\text{ch}} \mu_{\text{ch}} \Omega_0^2/c^2]^{1/2}$, and the sign absorbed into the aperture-overlap constants $C_{L,T}$. The estimate is not a substitute for a full-wave channel calculation; it displays the geometric quantities—aperture overlaps, channel length and radius, and the TE/TM cutoff hierarchy—that set the longitudinal/transverse balance and hence the proximity to the exact point $J_L = -J_T$.

Appendix C: Invariance criterion and the projected Hamiltonian

The longitudinal and transverse projectors $P_L = \hat{\mathbf{n}} \hat{\mathbf{n}}^\top$ and $P_T = \mathbf{I}_3 - \hat{\mathbf{n}} \hat{\mathbf{n}}^\top$ satisfy $P_L^2 = P_L$, $P_T^2 = P_T$, $P_L P_T = 0$, $P_L + P_T = \mathbf{I}_3$, so $\mathcal{J}(\hat{\mathbf{n}}) \mathbf{d} = J_L \mathbf{d}_L + J_T \mathbf{d}_T$: J_L is the channel-parallel and J_T the channel-perpendicular coupling. The geometric identities (10) follow directly from (1) and (4). For the off-sector map, expanding $\mathcal{J}(\hat{\mathbf{n}}_{uv}) \hat{\boldsymbol{\chi}}_v = J_T \hat{\boldsymbol{\chi}}_v + (J_L - J_T) (\hat{\mathbf{n}}_{uv} \hat{\boldsymbol{\chi}}_v) \hat{\mathbf{n}}_{uv}$ and using (10) gives Eq. (12); since $\hat{\mathbf{n}}_{uv} \not\parallel \hat{\boldsymbol{\chi}}_u$, the off-radial term vanishes on every bond iff $J_L + J_T = 0$, which is Eq. (13). For the projected block, $\hat{\boldsymbol{\chi}}_u^\top \mathcal{J}(\hat{\mathbf{n}}_{uv}) \hat{\boldsymbol{\chi}}_v = J_T (\hat{\boldsymbol{\chi}}_u \cdot \hat{\boldsymbol{\chi}}_v) + (J_L - J_T) (\hat{\boldsymbol{\chi}}_u \cdot \hat{\mathbf{n}}_{uv}) (\hat{\mathbf{n}}_{uv} \cdot \hat{\boldsymbol{\chi}}_v) = J_T (-\frac{1}{3}) + (J_L - J_T) (-\frac{2}{3}) = (J_T - 2J_L)/3 \equiv J_\chi$, and $\hat{\boldsymbol{\chi}}_u^\top \Sigma_u \hat{\boldsymbol{\chi}}_u = \Delta_\chi$, which assemble into Eq. (11). Because H_{sc} has two flat bands at $\lambda_{\text{sc}} = -2$, the projected sector has two flat branches at $\lambda_{\chi, \text{flat}} = \Delta_\chi - 2J_\chi$; these are exact vector flat bands precisely under the additional condition (13).

* phchan@ust.hk

† guoqh@hnu.edu.cn

- [1] D. Leykam, A. Andreanov, and S. Flach, “Artificial flat band systems: from lattice models to experiments,” *Adv. Phys. X* **3**, 1473052 (2018).
- [2] M. Röntgen, C. V. Morfonios, and P. Schmelcher, “Compact localized states and flat bands from local symmetry partitioning,” *Phys. Rev. B* **97**, 035161 (2018).
- [3] G. Morales-Pérez *et al.*, “Transversality-enforced tight-binding models for three-dimensional photonic crystals,” *Phys. Rev. B* **111**, 235206 (2025).

- [4] J. D. Joannopoulos, S. G. Johnson, J. N. Winn, and R. D. Meade, *Photonic Crystals: Molding the Flow of Light*, 2nd ed. (Princeton University Press, Princeton, 2008).
- [5] B. Bradlyn, L. Elcoro, J. Cano, M. G. Vergniory, Z. Wang, C. Felser, M. I. Aroyo, and B. A. Bernevig, “Topological quantum chemistry,” *Nature (London)* **547**, 298 (2017).
- [6] H. Watanabe and L. Lu, “Space group theory of photonic bands,” *Phys. Rev. Lett.* **121**, 263903 (2018).
- [7] T. Ozawa, H. M. Price, A. Amo, N. Goldman, M. Hafezi, L. Lu, M. C. Rechtsman, D. Schuster, J. Simon, O. Zilberberg, and I. Carusotto, “Topological photonics,” *Rev. Mod. Phys.* **91**, 015006 (2019).
- [8] J. D. Jackson, *Classical Electrodynamics*, 3rd ed. (Wiley, New York, 1999).
- [9] J. A. Stratton, *Electromagnetic Theory* (McGraw-Hill, New York, 1941).
- [10] C. F. Bohren and D. R. Huffman, *Absorption and Scattering of Light by Small Particles* (Wiley-Interscience, New York, 1983).
- [11] D. C. Tzarouchis, P. Ylä-Oijala, and A. Sihvola, “Resonant scattering characteristics of homogeneous dielectric sphere,” *IEEE Trans. Antennas Propag.* **65**, 3184 (2017).
- [12] R. E. Collin, *Foundations for Microwave Engineering*, 2nd ed. (Wiley-IEEE Press, New York, 2001).
- [13] D. M. Pozar, *Microwave Engineering*, 4th ed. (Wiley, Hoboken, NJ, 2011).
- [14] J. C. Slater, “Microwave electronics,” *Rev. Mod. Phys.* **18**, 441 (1946).
- [15] B. T. Draine and P. J. Flatau, “Discrete-dipole approximation for scattering calculations,” *J. Opt. Soc. Am. A* **11**, 1491 (1994).
- [16] M. A. Yurkin and A. G. Hoekstra, “The discrete dipole approximation: an overview and recent developments,” *J. Quant. Spectrosc. Radiat. Transfer* **106**, 558 (2007).
- [17] H. Wang, B. Yang, W. Xu, Y. Fan, Q. Guo, Z. Zhu, and C. T. Chan, “Highly degenerate photonic flat bands arising from complete graph configurations,” *Phys. Rev. A* **100**, 043841 (2019).
- [18] C. Xu, G. Wang, Z. H. Hang, J. Luo, C. T. Chan, and Y. Lai, “Design of full- k -space flat bands in photonic crystals beyond the tight-binding picture,” *Sci. Rep.* **5**, 18181 (2015).